

# Classical and quantum chaos in a circular billiard with a straight cut

Suhan Ree and L.E. Reichl

Center for Studies in Statistical Mechanics and Complex Systems  
The University of Texas at Austin, Austin, Texas 78712

(July 6, 1998)

We study classical and quantum dynamics of a particle in a circular billiard with a straight cut. This system can be integrable, nonintegrable with *soft* chaos, or nonintegrable with *hard* chaos, as we vary the size of the cut. We use a quantum web to show differences in the quantum manifestations of classical chaos for these three different regimes.

PACS numbers: 05.45.+b, 03.65.Ge, 02.70.Pt

## I. Introduction

In recent years, the dynamics of noninteracting particles in two-dimensional (2D) billiards has been studied in many different billiard shapes [1-6]. In this paper, we study the classical and quantum dynamics of a particle in a closed circular billiard with a straight cut (we name this system the “Moon” billiard; see Fig. 1). The classical system can exhibit both integrable and nonintegrable behavior. It also shows two distinct types of chaotic behavior, both “hard chaos” and “soft chaos” as we change the size of the cut. Systems whose dynamics consists of a mixture of stable and unstable periodic orbits are said to exhibit *soft* chaos. If all periodic orbits in a system are unstable throughout, the behavior is called *hard* chaos [7].

The quantum version of these billiards has a discrete energy spectrum, and chaos (or nonintegrability) manifests itself in the quantum billiard in indirect ways. The statistics of energy levels for classically integrable systems is different from that for classically chaotic systems [2-5,8-11], and one commonly uses the spectral statistics of energy levels as signature of an underlying chaos. Also discrete symmetries of the system should be handled carefully.

In this paper, we focus on a diagnostic tool which has proven successful for spin systems. We calculate the quantum web [11-14] using about a hundred lowest-energy eigenstates, and observe patterns for classically different cases. The lattice-structure, which appears for classically integrable cases, breaks in different ways for cases with soft chaos and hard chaos. The Husimi function [15,16], which extracts the quantum Poincaré section from a quantum state, is also calculated for some selected energy eigenstates to examine the quantum web more closely.

## II. The Classical Billiard

In this section, we focus on the classical dynamics of the Moon billiard. We introduce a dimensionless parameter  $w = W/R$  to characterize the system where  $W$  is the width of the billiard and  $R$  is the radius (see Fig. 1). Then we define  $M_w$  as a circular disk with a straight cut

with  $w$ . For example,  $M_2$  is a full circle and  $M_1$  is a half circle, and in general  $w$  is in the range of  $0 < w \leq 2$ . The classical Hamiltonian of a particle inside  $M_w$ , using polar coordinates  $(r, \theta)$ , is

$$H_w(r, \theta, p_r, p_\theta) = \frac{p_r^2}{2m} + \frac{p_\theta^2}{2mr^2} + V_w^R(r, \theta), \quad (1)$$

where  $V_w^R(r, \theta)$  represents the hard-wall potential of the billiard with radius  $R$  and  $W = wR$ . To begin, we will study the full circle ( $M_2$ ) and the half circle ( $M_1$ ). Both of cases are integrable. Then nonintegrable cases will be examined.

### A. Full-Circle Billiard, $M_2$

The dynamics of a particle inside  $M_2$  is integrable because there are two constants of motion, the energy  $E$  and the angular momentum  $p_\theta$ . Given  $E$  and  $p_\theta$ , the orbit lies on a 2D torus (2-torus) in phase space. There exists a canonical transformation to action-angle variables,  $(J_r, J_\theta, \phi_r, \phi_\theta)$ , where actions are given by

$$\begin{aligned} J_r &= \frac{\sqrt{2mE}}{\pi} \left[ \sqrt{R^2 - \frac{p_\theta^2}{2mE}} - \frac{|p_\theta|}{\sqrt{2mE}} \cos^{-1} \left( \frac{|p_\theta|}{R\sqrt{2mE}} \right) \right], \\ J_\theta &= p_\theta, \end{aligned} \quad (2)$$

with the new Hamiltonian  $H' = E(J_r, J_\theta)$ . We can also find the angle variables, but it should be noted that  $\phi_\theta$  is not equal to  $\theta$ . We can find explicit expressions of angular frequencies  $\dot{\phi}_r = \omega_r$  and  $\dot{\phi}_\theta = \omega_\theta$  as functions of  $E$  and  $p_\theta$  using Eq. (2),

$$\omega_r = \dot{\phi}_r = \frac{\partial E}{\partial J_r} = \left( \frac{\partial J_r}{\partial E} \right)^{-1} = \frac{2\pi E}{\sqrt{2mER^2 - p_\theta^2}}, \quad (3)$$

$$\begin{aligned} \omega_\theta &= \dot{\phi}_\theta = \frac{\partial E}{\partial J_\theta} = - \left( \frac{\partial J_r}{\partial J_\theta} \right) \left( \frac{\partial J_r}{\partial E} \right)^{-1} \\ &= \frac{\text{sgn}(p_\theta)}{\pi} \omega_r(E, p_\theta) \cos^{-1} \left( \frac{|p_\theta|}{R\sqrt{2mE}} \right). \end{aligned} \quad (4)$$

It is useful to look at periodic orbits (orbits for which the ratios of two angular frequencies are rational). We

classify periodic orbits using the notation  $(m, n)$  where  $m$  and  $n$  are relatively prime positive integers defined by

$$\left| \frac{\omega_\theta}{\omega_r} \right| = \frac{1}{\pi} \cos^{-1} \left( \frac{|p_\theta|}{R\sqrt{2mE}} \right) = \frac{m}{n}, \quad (5)$$

where  $2m < n$  [see Fig. 2(a)]. If we have a periodic orbit classified as  $(m, n)$ , an infinite number of rotated periodic orbits also belongs to  $(m, n)$ . Therefore periodic orbits in the full circle are *non-isolated* [1]. For any periodic orbit classified as  $(m, n)$ , there are  $n$  bounces and  $m$  revolutions in one cycle. On the other hand, a non-periodic orbit will not come back to the starting point, and eventually fill the whole 2-torus.

## B. Half-Circle Billiard, $M_1$

For the half circle, we still have two constants of motion,  $E$  and  $p_\theta^2$ . The range of  $\theta$  is reduced to a half,  $-\frac{\pi}{2} < \theta < \frac{\pi}{2}$ , but we can still construct 2-tori on which orbits lie. For any orbit in  $M_1$  there is a corresponding orbit in  $M_2$ . (If there is an orbit in  $M_2$ , folding  $M_2$  in half gives us a corresponding orbit in  $M_1$ .) Hence we can use the results found for  $M_2$  to describe some periodic orbits. A periodic orbit is classified as  $(m, n)'$  when the corresponding orbit in  $M_2$  is  $(m, n)$ . Unlike for  $M_2$ , periodic orbits in  $M_1$  are *isolated*, since there is no rotational symmetry. In the group  $(m, n)'$ , there are an infinite number of different periodic orbits, but only a few play an important role when  $w$  is slightly less than 1. In Fig. 2(b), those periodic orbits are shown. The stabilities of these periodic orbits are all neutral (neither stable nor unstable) like those in  $M_2$ .

It is useful to see periodic orbits in the space of  $E$  and  $|p_\theta|$ . A point in this space corresponds to a group of orbits with constants of motion  $E$  and  $p_\theta^2$ . When Eq. (5) is satisfied, the group consists of periodic orbits. Thus the condition to have periodic orbits is given by Eq. (5), and is plotted in Fig. 3. They are densely populated in the classically allowed region. The classically forbidden region in this space is given by  $E - p_\theta^2/(2mR^2) < 0$ . In integrable cases, orbits are a point (zero-dimensional) in  $(E, |p_\theta|)$ -space since  $E$  and  $p_\theta^2$  are conserved, but as the rotational symmetry breaks by changing  $w$ ,  $p_\theta^2$  is no longer conserved and orbits become one-dimensional. We will see later that Eq. (5) gives us the condition for primary resonances when  $w$  is slightly less than 1.

## C. $M_w$ when $0 < w < 1$ or $1 < w < 2$

Except two cases studied above ( $w = 1, 2$ ), the system is nonintegrable, because  $E$  is an only constant of motion in the system of two degrees of freedom. The stabilities of periodic orbits in  $M_w$  give us one way to understand the dynamical behavior of the system. The simplest periodic orbit for any  $w$  is an orbit with two bounces, going back and forth [for example,  $(1, 2)'$  in Fig. 2(b)]. To calculate

the stability of this orbit, we need to imagine a new billiard  $M_w^2$ , which is a composite of circular parts of two  $M_w$ 's facing each other. It is easy to see that  $M_1^2$  is just  $M_2$ . Orbits in  $M_w$  have the correspondence with orbits in  $M_w^2$  as orbits in  $M_1$  correspond to orbits in  $M_2 = M_1^2$ . The stability of this two-bounce orbit in  $M_w^2$  can be calculated from a  $2 \times 2$ -matrix  $\mathbf{m}$ , acting on  $(\delta\theta, \frac{\delta p_\theta}{R\sqrt{2mE}})$  on the boundary, which decides the deviation after two bounces [1]

$$\mathbf{m} = \begin{pmatrix} 2(2w-1)^2 - 1 & 4w(1-2w) \\ 4(2w-1)(1-w) & 2(2w-1)^2 - 1 \end{pmatrix}. \quad (6)$$

The eigenvalues of  $\mathbf{m}$ ,  $\lambda_\pm$ , are given in terms of the trace of  $\mathbf{m}$ ,

$$\lambda_\pm = \frac{1}{2} \left\{ \text{Tr } \mathbf{m} \pm [(\text{Tr } \mathbf{m})^2 - 4]^{1/2} \right\}, \quad (7)$$

where we used  $\det |\mathbf{m}| = 1$  since  $\mathbf{m}$  is area-preserving. The orbit is neutral when  $|\text{Tr } \mathbf{m}| = 2$ , stable when  $|\text{Tr } \mathbf{m}| < 2$ , and unstable when  $|\text{Tr } \mathbf{m}| > 2$ . The two-bounce orbit is neutral when  $w = 0.5$ ,  $w = 1$ , or  $w = 2$ , stable when  $0 < w < 0.5$  or  $0.5 < w < 1$ , and unstable when  $1 < w < 2$ . We have seen that all periodic orbits are neutral when the system is integrable ( $w = 1, 2$ ) but  $w = 0.5$  is a special case as we will see later. From this result, we can predict that there are no stable periodic orbits in the billiard  $M_{1 < w < 2}$ , and periodic orbits in  $M_{0 < w < 1}$  are either stable or unstable, except when  $w = 0.5$ . (Ergodicity of the billiard  $M_{1 < w < 2}$  has been proven by Bunimovich [17].) The system shows hard chaos when  $1 < w < 2$ , and soft chaos when  $0 < w < 1$ .

The Poincaré surface of section (PSS) is one way to observe the chaos. Here PSS is a two-dimensional surface  $(\theta, p_\theta)$  at  $r = R$  along the circular boundary  $(-\theta_{max} < \theta < \theta_{max}, -R\sqrt{2mE} < p_\theta < R\sqrt{2mE})$ . Each orbit gives a point in  $(\theta, p_\theta)$ -space every time it touches this surface. Therefore PSS becomes a 2D area-preserving map. In fully chaotic (ergodic) cases, points generated by an orbit will fill out the whole allowed space in the PSS. In cases of soft chaos, we observe some structure. Some orbits generate island chains and some orbits will fill some remaining regions in a chaotic manner. Since the KAM theorem [7,11] does not apply in this system due to singularities of the boundary, the existence of KAM tori separating island chains is not guaranteed even for small  $\delta$  when  $w = 1 - \delta$ .

In Fig. 4, we show PSS's for various  $w$ 's. In Fig. 4(a), one orbit is filling the whole region when  $w = 1.01$ . This is a fully chaotic case. Figure 4(b) is an integrable case when  $w = 1$ . When  $w = 0.99$  [Fig. 4(c)], we see island chains centered at the positions of periodic orbits along with stochastic diffusion in the remaining region. The resonance condition, Eq. (5), gives us locations of island chains. For example,  $(1, 2)'$  gives us the location  $p_\theta/(R\sqrt{2mE}) = 0$ ,  $(1, 4)'$  gives us  $p_\theta/(R\sqrt{2mE}) = \pm 1/\sqrt{2}$ ,  $(1, 3)'$  gives us  $p_\theta/(R\sqrt{2mE}) = \pm 0.5$ , and  $(1, 6)'$  gives us  $p_\theta/(R\sqrt{2mE}) = \pm\sqrt{3}/2$ , and so on. As  $w$  decreases [Figs. 4(d) and 4(e)], we see increasing chaotic

region and some remaining island chains. When  $w = 0.5$  [Fig. 4(f)], periodic orbits that have neutral stabilities reside in two axes,  $(\theta = 0)$ -axis and  $(p_\theta = 0)$ -axis. One orbit starting near the center is filling out almost all region. This is the most chaotic case when  $0 < w < 1$ . As  $w$  decreases further, we see bigger regular regions in PSS in Figs. 4(g) and 4(h).

### III. The Quantum Billiard

In this section, we study the quantized  $M_w$ -billiard using a quantum-web analysis with about a hundred lowest-energy eigenstates, and we also look at some individual energy eigenstates using Husimi plots.

#### A. Numerical Method

The Schrödinger equation for this 2D  $M_w$ -billiard is the Helmholtz equation,

$$(\nabla^2 + k^2)\Psi(\mathbf{r}) = 0, \quad (8)$$

with the Dirichlet boundary condition,  $\Psi = 0$ , on the boundary of  $M_w$ ,  $B_w \equiv \partial M_w$ , where  $k^2 = 2mE/\hbar^2$  and  $\nabla^2 = \frac{\partial^2}{\partial r^2} + \frac{1}{r}\frac{\partial}{\partial r} + \frac{1}{r^2}\frac{\partial^2}{\partial \theta^2}$  using polar coordinates.

For the classically integrable cases, this equation can be solved analytically. The Hamiltonian  $\hat{H}_w$  ( $w = 1$  or  $2$ ) and the angular momentum  $\hat{p}_\theta$  ( $\hat{p}_\theta^2$  for the half circle) commute. They are generators of continuous symmetry transformations, the time translation and the rotation. For a full circle  $M_2$ , we can find energy eigenstates which are simultaneous eigenstates of  $\hat{H}_2$  and  $\hat{p}_\theta$ ,

$$\langle \mathbf{r}|l, k\rangle^{(f)} \propto J_l\left(\frac{\alpha_{lk}r}{R}\right) e^{il\theta}, \quad (9)$$

where  $k$  is a positive integer,  $l$  is an integer, and  $\alpha_{lk}$  is the  $k$ th zero of the Bessel function  $J_l(x)$ . And energy levels are given by  $E_{lk}^{(f)} = \hbar^2\alpha_{lk}^2/(2mR^2)$ . There exist two-fold degeneracies when  $l \neq 0$  since the system also has the parity symmetry and  $[\hat{p}_\theta, \hat{P}] \neq 0$  ( $\hat{P}$  is the parity operator). Then we can find another set of energy eigenstates, simultaneous eigenstates of  $\hat{H}_2$ ,  $\hat{p}_\theta^2$ , and  $\hat{P}$ ,

$$\begin{aligned} \langle \mathbf{r}|l, k, +\rangle^{(f)} &\propto J_l\left(\frac{\alpha_{lk}r}{R}\right) \cos(l\theta) \quad (l \geq 0), \\ \langle \mathbf{r}|l, k, -\rangle^{(f)} &\propto J_l\left(\frac{\alpha_{lk}r}{R}\right) \sin(l\theta) \quad (l \geq 1), \end{aligned} \quad (10)$$

where  $-\pi < \theta < \pi$ . The latter will be used in the calculation of the quantum web.

For a half circle  $M_1$ , energy levels are the same as those of the full circle without levels with  $l = 0$ , and the energy eigenfunctions are

$$\begin{aligned} \langle \mathbf{r}|l, k, +\rangle^{(h)} &\propto J_l\left(\frac{\alpha_{lk}r}{R}\right) \cos(l\theta) \quad (l = 1, 3, 5, \dots), \\ \langle \mathbf{r}|l, k, -\rangle^{(h)} &\propto J_l\left(\frac{\alpha_{lk}r}{R}\right) \sin(l\theta) \quad (l = 2, 4, 6, \dots), \end{aligned} \quad (11)$$

where  $-\pi/2 < \theta < \pi/2$ . Here there is no degeneracy.

For classically nonintegrable cases,  $\hat{p}_\theta^2$  no longer commutes with  $\hat{H}_w$  (but still  $[\hat{P}, \hat{H}_w] = 0$  for any  $w$ ). Here

Eq. (8) must be solved numerically. We use the boundary element method (BEM) [2,18-20] to solve this nonseparable 2D partial differential equation. It is an efficient way to solve boundary-value problems, because in BEM a 2D equation with boundary condition becomes an integral equation in one variable along the boundary. The method we use is briefly outlined below.

We use a Green's function,  $G(\mathbf{r}, \mathbf{r}') = -\frac{i}{4}H_0^{(1)}(k|\mathbf{r} - \mathbf{r}'|)$ , which satisfies

$$(\nabla^2 + k^2)G(\mathbf{r}, \mathbf{r}') = \delta(\mathbf{r} - \mathbf{r}'), \quad (12)$$

where  $H_i^{(1)}(x)$  is the Hankel function of the first kind. We multiply Eq. (8) by  $G(\mathbf{r}, \mathbf{r}')$ , and multiply Eq. (12) by  $\Psi(\mathbf{r}')$ . After subtracting one from the other, integrating over the area of  $M_w$  with respect to  $\mathbf{r}'$ , and using Green's theorem, we finally get

$$-\oint_{B_w} ds' G(\mathbf{r}, \mathbf{r}') u(s') = \begin{cases} \Psi(\mathbf{r}), & \mathbf{r} \text{ inside } B_w, \\ \frac{1}{2}\Psi(\mathbf{r}), & \mathbf{r} \text{ on } B_w, \\ 0, & \mathbf{r} \text{ outside } B_w, \end{cases} \quad (13)$$

where  $s'$  is arc-length along  $B_w = \partial M_w$ ,  $u(s') \equiv \mathbf{n}' \cdot \nabla' \Psi(\mathbf{r}(s'))$ , and  $\mathbf{n}'$  is the outward normal unit vector to  $B_w$  at  $\mathbf{r}'$ . With  $\mathbf{r}$  lying on  $B_w$ , by taking the normal derivative  $\mathbf{n} \cdot \nabla$  on both sides of Eq. (13), we obtain

$$u(s) = -2 \oint_{B_w} ds' u(s') (\mathbf{n} \cdot \nabla) G(\mathbf{r}, \mathbf{r}'). \quad (14)$$

One way to solve this equation is discretizing  $B_w$  by dividing it into  $N$  segments. Then Eq. (14) becomes the matrix equation  $\mathbf{A} \cdot \mathbf{x} = \mathbf{x}$ , where  $\mathbf{A} = \mathbf{A}(k)$  is an  $(N \times N)$ -matrix and  $\mathbf{x}$  is an  $N$ -component vector representing  $\{u(s_i) | 1 \leq i \leq N\}$ . For given  $w$ , energy levels of the system,  $E_n = \hbar^2 k_n^2 / 2m$  ( $n \geq 1$ ), can be found by solving the equation,  $\det[\mathbf{A}(k) - \mathbf{I}] = 0$ . For each energy level  $E_n$ , we can obtain  $\{u_n(s_i)\}$  by finding an eigenvector of  $\mathbf{A}(k_n)$  with a near-zero eigenvalue. Since the numerically obtained energy levels in this way always have some uncertainty, "degeneracy" (which is actually near-degeneracy) can occur when the difference between two adjacent exact energy levels is less than the uncertainty. In these cases, we can find two sets of  $\{u(s_i)\}$  with two near-zero eigenvalues of  $\mathbf{A}$ . Therefore, looking at eigenvalues of  $\mathbf{A}(k_n)$  can be an easy way to check numerically for near-degeneracies of an energy level,  $E_n$ .

For given  $w$ , we found energy levels  $\{E_n | n \geq 1\}$  and normal derivatives, on the boundary, of corresponding energy eigenfunctions  $\{\Psi_n(\mathbf{r}) \equiv \langle \mathbf{r}|n\rangle\}$  where  $|n\rangle$ 's are energy eigenstates. Then from Eq. (13) we can calculate the energy eigenfunction inside,

$$\Psi_n(\mathbf{r}) = \frac{i}{4} \oint_{B_w} ds' H_0^{(1)}(k_n |\mathbf{r} - \mathbf{r}'|) u_n(s'). \quad (15)$$

Using Eq. (15), we can also calculate  $\langle \mathbf{r} | \hat{p}_\theta^2 | n \rangle$ , which will be used in calculations of quantum webs in the next subsection,

$$\begin{aligned} \langle \mathbf{r} | \hat{p}_\theta^2 | n \rangle &= -\hbar^2 \frac{\partial^2}{\partial \theta^2} \Psi_n(\mathbf{r}) \\ &= \frac{i}{4} \oint_{B_w} ds' \left[ \frac{\partial^2}{\partial \theta^2} H_0^{(1)}(k_n |\mathbf{r} - \mathbf{r}'|) \right] u_n(s'), \end{aligned} \quad (16)$$

where

$$\begin{aligned} \frac{\partial^2}{\partial \theta^2} H_0^{(1)}(k |\mathbf{r} - \mathbf{r}'|) &= k \left[ \frac{\partial^2}{\partial \theta^2} |\mathbf{r} - \mathbf{r}'| \right] H_0^{(1)'}(k |\mathbf{r} - \mathbf{r}'|) \\ &\quad + k^2 \left[ \frac{\partial}{\partial \theta} |\mathbf{r} - \mathbf{r}'| \right]^2 H_0^{(1)''}(k |\mathbf{r} - \mathbf{r}'|), \end{aligned} \quad (17)$$

and we use

$$|\mathbf{r} - \mathbf{r}'| = \sqrt{(r \cos \theta - x')^2 + (r \sin \theta - y')^2}, \quad (18)$$

and

$$\begin{aligned} H_0^{(1)'}(x) &= -H_1^{(1)}(x), \\ H_0^{(1)''}(x) &= -H_0^{(1)}(x) + \frac{H_1^{(1)}(x)}{x}. \end{aligned} \quad (19)$$

In calculations of  $\Psi_n$  and  $\frac{\partial^2}{\partial \theta^2} \Psi_n$ , care must be taken when  $\mathbf{r}$  is close to the boundary because  $H_i^{(1)}(|\mathbf{r} - \mathbf{r}'|)$  diverges as  $|\mathbf{r} - \mathbf{r}'|$  goes to zero.

## B. The Quantum Web

The quantum-web analysis can be used to observe the manifestations of classical chaos in quantum mechanics, and until now has been used primarily in spin systems [13,14]. Here we will look at three different cases: classically integrable cases ( $w = 1, 2$ ), nonintegrable cases showing soft chaos ( $0 < w < 1$ ), and nonintegrable cases with hard chaos ( $1 < w < 2$ ).

For classically integrable cases ( $w = 1, 2$ ), we have seen in Sec. II that there are two constants of motion,  $E$  and  $|p_\theta|$ , and that we can find two action variables  $(J_r, J_\theta)$ . (There exists a nonlinear map from  $(J_r, J_\theta)$ -space to  $(E, |p_\theta|)$ -space.) In Fig. 3, a classical orbit appears as a point in  $(E, |p_\theta|)$ -space. In quantum mechanics, there exist simultaneous eigenstates of two operators  $\hat{H}_w$  ( $w = 1$  or  $2$ ) and  $\hat{p}_\theta^2$  [see Eqs. (10) and (11)]. We can construct a 2D space, in which a pair of eigenvalues  $(E_{lk}, |l\hbar|)$  of each eigenstate is plotted as a point. In Figs. 5(e) and 5(l), we observe the structure of a deformed lattice. This can be understood as a mapping from an almost perfect 2D lattice in  $(J_r, J_\theta)$ -space to the deformed lattice in  $(E, |p_\theta|)$ -space. This almost perfect lattice-structure can be explained from Einstein-Brillouin-Keller (EBK) semiclassical quantization,

$$\begin{aligned} J_r &\simeq (n_r - \frac{1}{4})\hbar \quad (n_r : \text{positive integer}), \\ J_\theta &= p_\theta = l\hbar \quad (l : \text{integer}), \end{aligned} \quad (20)$$

where  $J_r$  is a very good approximation and  $J_\theta$  is exact. This is the quantum analogue of Fig. 3. Each point in

Fig. 3 represents a 2-torus. Thus, we can find a 2-torus in classical phase space corresponding to a quantum eigenstate, and then each eigenstate here corresponds to a group of orbits that are on this 2-torus.

For classically nonintegrable cases,  $[\hat{p}_\theta^2, \hat{H}_w] \neq 0$  when  $w \neq 1$  or  $2$ . However, we can still calculate an expectation value of  $\hat{p}_\theta^2$  for an energy eigenstate  $|n\rangle$ ,  $\langle n | \hat{p}_\theta^2 | n \rangle$ , numerically using Eqs. (15) and (16),

$$\begin{aligned} \langle n | \hat{p}_\theta^2 | n \rangle &= \int_{M_w} d^2 \mathbf{r} \langle n | \mathbf{r} \rangle \langle \mathbf{r} | \hat{p}_\theta^2 | n \rangle \\ &= -\hbar^2 \int_{M_w} d^2 \mathbf{r} \Psi_n^*(\mathbf{r}) \frac{\partial^2 \Psi_n(\mathbf{r})}{\partial \theta^2}. \end{aligned} \quad (21)$$

These values can be interpreted as time-averages of  $\hat{p}_\theta^2$  [12]. When there is an accidental degeneracy (or near-degeneracy), we find expectation values from eigenvalues of the matrix representation of  $\hat{p}_\theta^2$  in the degenerate subspace. In this way, we obtain a pair of values  $(E_n, \sqrt{\langle n | \hat{p}_\theta^2 | n \rangle})$  for each energy eigenstate. These points can also be plotted in a 2D space as a quantum web. We expect that the lattice-structure that exists for integrable cases will be broken because EBK quantization doesn't apply to nonintegrable cases.

In Figs. 5(a)-5(d), quantum webs are shown for cases of soft chaos. When  $w = 0.99$  [Fig. 5(d)], we observe breaking of the web near conditions of primary resonances in classical mechanics. We see patterns of crossing near  $(1, 4)'$ - and  $(1, 3)'$ -resonances. Although "regular" parts still exist, some layers seem to start to shift near resonance conditions. We can roughly estimate the energy value at which the effect starts to be seen for each resonance condition by measuring the width of island chains,  $\Delta p_\theta$ , in Fig. 4(d). For example,  $(1, 2)'$ -resonance has the biggest width, and next  $(1, 4)'$ -resonance, and so on. Because  $p_\theta$  is scaled by  $(R\sqrt{2mE})^{-1}$  in Fig. 4,  $\Delta p_\theta$  is proportional to  $\sqrt{E}$ . When  $\Delta p_\theta (= \Delta J_\theta) \geq \hbar$ , the resonance can be clearly seen in the quantum system, and we can roughly obtain an estimate of the minimum energy at which each resonance is in effect. The smaller the width of an island chain and the lower the energy, the less likely to find the web broken near the curve of the particular resonance. When  $w = 0.7$  [Fig. 5(c)], we see similar patterns as in Fig. 5(d). When  $w = 0.5$  [Fig. 5(b)], the classical system has a large chaotic region in the PSS, and has periodic orbits with neutral stability, which reside on two axes,  $\theta = 0$  and  $p_\theta = 0$ . The quantum web, however, is quite regular although the structure looks different from those of integrable cases. It looks more like a structure of layers. When  $w = 0.3$  [Fig. 5(a)], the web is similar to that of Fig. 5(b).

In Figs. 5(f)-(k), we show quantum webs for cases of hard chaos. When  $w = 1.01$  [Fig. 5(f)], the lattice-structure is still intact except a little kink, although this is the fully chaotic case classically [see Fig. 4(a)]. We

observe the lattice-structure quickly collapses as we increase  $w$ . When  $w = 1.5$  [Fig. 5(i)], the structure is very irregular except for four regularly placed points near the top-right corner. (Some of eigenstates noted by arrows here will be examined in the next subsection using Husimi plots.) The case of  $w = 1.7$  [Fig. 5(j)] is the most irregular quantum web among cases shown. When  $w = 1.9$  [Fig. 5(k)], we observe splitting of degeneracies and also quick collapse of lattice-structure from an integrable case  $w = 2$  [Fig. 5(l)]. As we have seen so far, the lattice structure tends to collapse quickly irrespective of energy in cases of hard chaos, but there also exist small remnants of regularity in some cases.

### C. Quantum Poincaré Section

The Husimi plot provides a method of extracting a quantum Poincaré surface of section (QPS) from a quantum state [15]. The QPS is a quantum analogue of PSS, which we have obtained in Sec. II. The Husimi function of an 1D system corresponding to a state  $|\Psi\rangle$  is defined as

$$F(x_0, p_0) = |\langle x_0, p_0 | \Psi \rangle|^2, \quad (22)$$

where  $|x_0, p_0\rangle$  is a coherent state with a representation in configuration space,

$$\langle x | x_0, p_0 \rangle = \left( \frac{1}{\pi\sigma^2} \right)^{\frac{1}{4}} \exp \left[ -\frac{(x - x_0)^2}{2\sigma^2} + \frac{i}{\hbar} p_0 (x - x_0) \right]. \quad (23)$$

In 2D billiards, Eq. (22) can be modified to create a Husimi function using the coordinate along the boundary [16]. For example, for  $M_w$ -billiard along the circular part of the boundary, the Husimi function is defined as

$$F_n(\theta_0, p_{\theta 0}) = \left| \int_{-\theta_{max}}^{\theta_{max}} d\theta' \langle \theta_0, p_{\theta 0} | \theta' \rangle u_n(\theta') \right|^2, \quad (24)$$

where  $-\theta_{max} < \theta_0 < \theta_{max}$  and  $-R\sqrt{2mE} < p_{\theta 0} < R\sqrt{2mE}$ . Here  $\langle \theta' | \theta_0, p_{\theta 0} \rangle$  has the same form as in Eq. (23) with  $\sigma$  given by the value  $[\theta_{max}\hbar/(R\sqrt{2mE})]^{1/2}$ , and  $u_n(\theta)$  is the normal derivative of the energy eigenfunction on the circular part of the boundary,  $\frac{\partial}{\partial r}\Psi_n(\mathbf{r})|_{r=R}$ .

In Fig. 6, we show Husimi plots for selected eigenstates for three cases ( $w = 0.5, 0.9, 1.5$ ). And, in Fig. 7, we show probability densities of wave functions,  $|\Psi_n(\mathbf{r})|^2$ , for some of eigenstates chosen from Fig. 6. (Most eigenstates chosen in Fig. 6 can be found in Figs. 5(b), 5(d), and 5(i) with arrows pointed to them.)

Figures 6(a)-6(d) show Husimi plots of energy eigenstates when  $w = 0.5$ . The pattern of PSS shown in Fig. 4(f) can be seen in these plots. We can get some information on chosen eigenstates from the quantum web [Fig. 5(b)]. The eigenstate for Fig. 6(a) is on the outer part, and the eigenstate for Fig. 6(b) is on the inner part of the quantum web. Figure 6(a) shows chaotic region of PSS, and Fig. 6(b) seems to correspond with a two-bounce

orbit with neutral stability, which we can observe in the wave function [Fig. 7(a)]. The eigenstate for Fig. 6(c) is in the middle of the quantum web, and its Husimi plot and wave function [Fig. 7(b)] lie between two extreme cases above. The eigenstate for Fig. 6(d) has a relatively high energy, but the structure is similar to Fig. 6(c).

Figures 6(e)-6(h) show Husimi plots of energy eigenstates when  $w = 0.9$ , and each eigenstate is picking up a classical primary resonance shown as an island chain in PSS [Fig. 4(d)]. The eigenstate for Fig. 6(e), located near the  $(1, 2)'$ -resonance in the quantum web [Fig. 5(d)], shows the pattern of the island chain of the  $(1, 2)'$ -resonance, although it is only the 9th highest energy eigenstate. The eigenstates of Figs. 6(f) and 6(g), located at the crossing of two layers near the  $(1, 4)'$ -resonance, show the pattern of the island chain of the  $(1, 4)'$ -resonance. Wave functions [Figs. 7(c) and 7(d)] of these states show the trace of unstable and stable periodic orbits [see Fig. 2(b)], respectively. The eigenstate for Fig. 6(h), which is on the  $(1, 3)'$ -resonance, also shows the pattern of the island chain of the  $(1, 3)'$ -resonance. As expected earlier, the  $(1, 2)'$ -resonance is observed in the Husimi plot at lower-energy eigenstates than the  $(1, 4)'$ -resonance.

Figures 6(i)-6(l) show Husimi plots of energy eigenstates when  $w = 1.5$ . The eigenstate for Fig. 6(i), located in the inner part of the quantum web [Fig. 5(i)], seems to be picking up the periodic orbit with neutral stability, which can be seen clearly in the wave function [Fig. 7(e)]. The eigenstate of Fig. 6(k), which is one of four regularly placed points in the quantum web, shows a *whispering gallery* state [Fig. 7(f)]. All four of these regularly placed eigenstates show similar Husimi plots. A relatively high energy eigenstate for Fig. 6(l) shows a more uniformly distributed Husimi plot like the corresponding PSS in classical mechanics.

## IV. Conclusions

The quantum web is the quantum representation of  $(E, |p_{\theta}|)$ -space in Fig. 3. In the regime of soft chaos, we observe that the lattice-structure obtained for the integrable case starts to break near the primary resonance conditions obtained from classical mechanics as the width parameter,  $w$ , decreases from  $w = 1$ . The effect of resonances is greater when energy is higher and the width of an island chain in the PSS is greater. Even for the most chaotic case in the soft-chaos regime, layer-structure remains. In the hard-chaos regime, the regular quantum web collapses more quickly regardless of energy as the width parameter,  $w$ , increases from  $w = 1$ .

## Acknowledgments

The authors wish to thank the Welch Foundation, Grant No.F-1051, NSF Grant No.INT-9602971, and DOE

contract No.DE-FG03-94ER14405 for partial support of this work. We thank NPACI and the University of Texas High Performance Computing Center for use of its facilities.

## References

- [1] M. V. Berry, Eur. J. Phys. **2**, 91 (1981)
- [2] M. V. Berry and M. Wilkinson, Proc. R. Soc. London Ser. A **392**, 15 (1984)
- [3] M. Robnik, J. Phys. A: Math. Gen. **17**, 1049 (1984)
- [4] M. V. Berry, Ann. Phys. (N.Y.) **131**, 163 (1981)
- [5] S. W. McDonald and A. N. Kaufman, Phys. Rev. Lett. **42**, 1189 (1979); Phys. Rev. A **37**, 3067 (1988)
- [6] E. J. Heller, Phys. Rev. Lett. **53**, 1515 (1984)
- [7] M. C. Gutzwiller, *Chaos in Classical and Quantum Mechanics* (Springer-Verlag, New York, 1990)
- [8] I. C. Percival, J. Phys. B **6**, L229 (1973)
- [9] M. V. Berry and M. Tabor, Proc. R. Soc. London Ser. A **356**, 375 (1977)
- [10] O. Bohigas, M. J. Giannoni, and C. Schmit, Phys. Rev. Lett. **52**, 1 (1984)
- [11] L. E. Reichl, *The Transition to Chaos In Conservative Classical Systems: Quantum Manifestations* (Springer-Verlag, New York, 1992)
- [12] A. Peres, Phys. Rev. Lett. **53**, 1711 (1984)
- [13] N. Srivastava and G. Müller, Z. Phys. B **81**, 137 (1990); N. Srivastava, C. Kaufman, and G. Müller, J. Appl. Phys. **67**, 5627 (1990)
- [14] D. T. Robb and L. E. Reichl, Phys. Rev. E **57**, 2458 (1998)
- [15] K. Husimi, Proc. Phys. Math. Soc. Jpn. **22**, 246 (1940)
- [16] B. Crespi, G. Perez, and S. J. Chang, Phys. Rev. E **47**, 986 (1993)
- [17] L. A. Buminovich, Commun. Math. Phys. **65**, 295 (1979); Funct. Anal. Appl. **8**, 73 (1974)
- [18] G. R. C. Tai and R. P. Shaw, J. Acoust. Soc. Am. **56**, 796 (1974)
- [19] N. Kishi and T. Okoshi, IEEE Trans. Microwave Theory Tech. **MTT-35**, 887 (1987)
- [20] P. A. Knipp and T. L. Reinecke, Phys. Rev. B **54**, 1880 (1996)

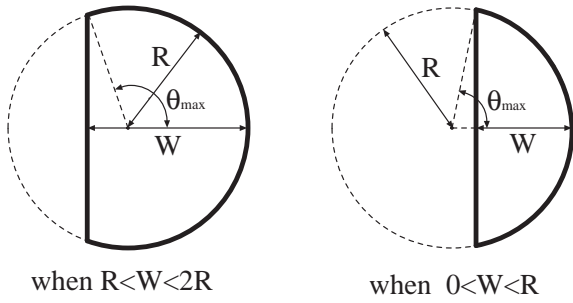


Figure 1: Geometry of the “Moon” billiard. When  $W = 2R$ , it is a full circle, and when  $W = R$ , it is a half circle. Here  $\theta_{max}$  is given by the equation,  $\cos \theta_{max} = (R - W)/R$ .

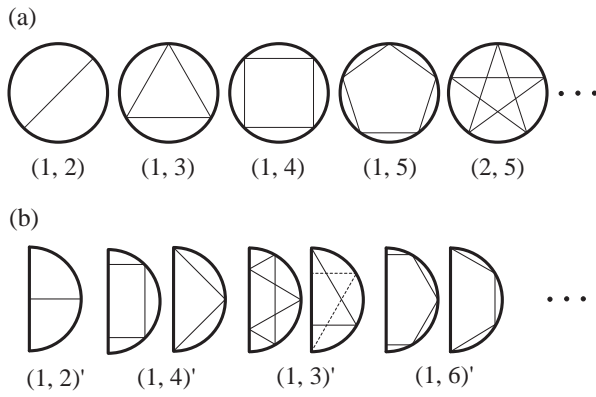


Figure 2: Closed orbits in integrable cases. (a) In a full circle, periodic orbits can be classified as  $(m, n)$  where orbits have  $m$  bounces and  $n$  revolutions in a cycle. (b) In a half circle, we can use the notation of a full circle to classify periodic orbits as  $(m, n)'$ .

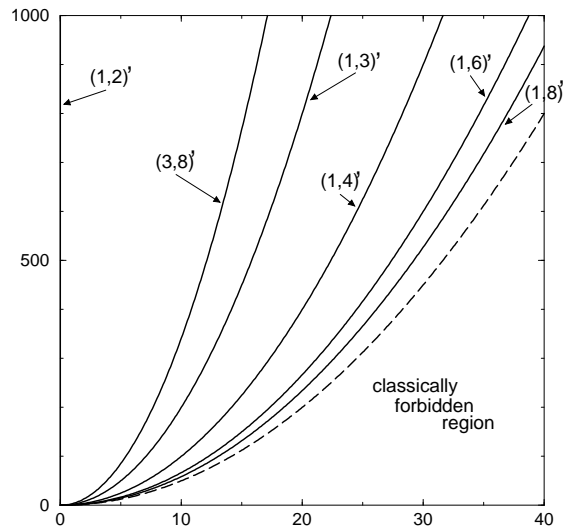


Figure 3: For a half circle, the condition in  $(E, |p_\theta|)$ -space to have periodic orbits  $(m, n)'$  is given by Eq. (5), and some are plotted. These curves are densely populated in classically allowed region.

Figure 4: The Poincaré surface of section of  $M_w$ -billiard varying  $w$  where  $w = W/R$ . We observe ergodic motions when  $1 < w < 2$ , and generic chaotic behaviors when  $0 < w < 1$ . (a) Ergodic when  $w = 1.01$  with one orbit. (b) Integrable when  $w = 1$ . (c)  $w = 0.99$ . (d)  $w = 0.9$ . (e)  $w = 0.7$ . (f)  $w = 0.5$ . Closed orbits residing in  $(\theta = 0)$ -axis and  $(p_\theta = 0)$ -axis have neutral stabilities. One orbit is filling almost all space except two axes. (g)  $w = 0.3$ . (h)  $w = 0.1$ .

Figure 6: Husimi plots for given eigenstates. ( $\epsilon \equiv E/(\frac{\hbar^2}{mR^2})$ ) (a)  $w = 0.5$  and  $\epsilon = 143.28$ . (b)  $w = 0.5$  and  $\epsilon = 740.79$ . (c)  $w = 0.5$  and  $\epsilon = 1156.07$ . (d)  $w = 0.5$  and  $\epsilon = 9992.23$ . (e)  $w = 0.9$  and  $\epsilon = 62.513$ . (f)  $w = 0.9$  and  $\epsilon = 365.64$ . (g)  $w = 0.9$  and  $\epsilon = 371.99$ . (h)  $w = 0.9$  and  $\epsilon = 617.98$ . (i)  $w = 1.5$  and  $\epsilon = 258.03$ . (j)  $w = 1.5$  and  $\epsilon = 284.94$ . (k)  $w = 1.5$  and  $\epsilon = 268.80$ . (l)  $w = 1.5$  and  $\epsilon = 842.69$ . [A square at the top right corner of each plot represents the size of  $\hbar$  (Planck constant). All eigenstates except (d) and (l) are pointed in quantum webs in Fig. 5 by arrows.]

Figure 5: The quantum web of  $M_w$ -billiard varying  $w$ . Even and odd parity eigenstates are shown together. (a)  $w = 0.3$ . (b)  $w = 0.5$ . (c)  $w = 0.7$ . (d)  $w = 0.9$ . The condition of primary resonances in classical mechanics are also shown. (e)  $w = 1.0$ . Classically integrable case. (f)  $w = 1.01$ . (g)  $w = 1.1$ . (h)  $w = 1.3$ . (i)  $w = 1.5$ . (j)  $w = 1.7$ . (k)  $w = 1.9$ . (l)  $w = 2.0$ . Classically integrable case. There are two-fold degeneracies when  $p_\theta \neq 0$ . [Arrows in (b), (d), and (i) indicate states which will be studied using Husimi plots in Fig. 6.]

Figure 7: The probability density of some energy eigenstates. ( $\epsilon \equiv E/(\frac{\hbar^2}{mR^2})$ ) (a)  $w = 0.5$  and  $\epsilon = 740.79$ . [See Fig. 6(b).] (b)  $w = 0.5$  and  $\epsilon = 1156.07$ . [See Fig. 6(c).] (c)  $w = 0.9$  and  $\epsilon = 365.64$ . [See Fig. 6(f).] (d)  $w = 0.9$  and  $\epsilon = 371.99$ . [See Fig. 6(g).] (e)  $w = 1.5$  and  $\epsilon = 258.03$ . [See Fig. 6(i).] (f)  $w = 1.5$  and  $\epsilon = 268.80$ . [See Fig. 6(k).]



This figure "figure4.gif" is available in "gif" format from:

<http://arxiv.org/ps/chao-dyn/9807018v1>

This figure "figure5.gif" is available in "gif" format from:

<http://arxiv.org/ps/chao-dyn/9807018v1>

This figure "figure6.gif" is available in "gif" format from:

<http://arxiv.org/ps/chao-dyn/9807018v1>

This figure "figure7.gif" is available in "gif" format from:

<http://arxiv.org/ps/chao-dyn/9807018v1>